A fast algorithm for Direct Numerical Simulation of natural convection flows in arbitrarily-shaped periodic domains

2015 J. Phys.: Conf. Ser. 655 012054

(http://iopscience.iop.org/1742-6596/655/1/012054)

Journal of Physics: Conference Series **655** (2015) 012054 doi:10.1088/1742-6596/655/1/012054

A fast algorithm for Direct Numerical Simulation of natural convection flows in arbitrarily-shaped periodic domains

D Angeli[1], E Stalio[2], M A Corticelli[2], and G S Barozzi[2]

[1] Dipartimento di Scienze e Metodi dell'Ingegneria, Università degli Studi di Modena e Reggio Emilia, Via Amendola 2, 42122 Reggio Emilia (Italy)
[2] Dipartimento di Ingegneria Enzo Ferrari, Università degli Studi di Modena e Reggio Emilia, Via Vivarelli 10, 41125 Modena (Italy)

E-mail: diego.angeli@unimore.it

Abstract. A parallel algorithm is presented for the Direct Numerical Simulation of buoyancy-induced flows in open or partially confined periodic domains, containing immersed cylindrical bodies of arbitrary cross-section. The governing equations are discretized by means of the Finite Volume method on Cartesian grids. A semi-implicit scheme is employed for the diffusive terms, which are treated implicitly on the periodic plane and explicitly along the homogeneous direction, while all convective terms are explicit, via the second-order Adams-Bashfort scheme. The contemporary solution of velocity and pressure fields is achieved by means of a projection method. The numerical resolution of the set of linear equations resulting from discretization is carried out by means of efficient and highly parallel direct solvers. Verification and validation of the numerical procedure is reported in the paper, for the case of flow around an array of heated cylindrical rods arranged in a square lattice. Grid independence is assessed in laminar flow conditions, and DNS results in turbulent conditions are presented for two different grids and compared to available literature data, thus confirming the favorable qualities of the method.

1. Introduction and scope

Direct Numerical Simulation (DNS) is a powerful research tool for the analysis of turbulent flows. As soon as care is taken in the choice of spatial and temporal discretization schemes, and grids or modal expansion truncations are adequate, DNS allows for a full 3D representation of all the turbulent scales of a flow in a set of time steps, from which a large amount of information can be extracted on the nature of the simulated turbulent flow [1].

Although the continuous increase in available computing resources has made it possible to achieve results at very high Reynolds numbers [2] or with extremely refined grids [3], DNSs are often limited to flows in very simple domains, like channels, pipes or flat plates, mainly due to the limitations of certain discretization methods (e.g. spectral methods) or to the numerical errors that might affect the resolution of the discrete equations on unstructured grids, typically involving an excessive amount of unphysical artificial diffusion, which introduces large errors in the representation of the smallest scales of the flow. For this reason, novel parallel and accurate methods for the DNS of flows in complex geometries are still a relevant topic in the field of computational fluid dynamics.

In this context, the approaches based on the representation of arbitrary domains in the frame of a Finite Difference or Finite Volume Cartesian grid, commonly known as Immersed Boundary Methods, are among the most attractive, given the ease in generating the mesh and the possibility of a straightforward parallelization. Stemming from the original development of the Immersed Boundary Method by Peskin [4], a variety of different methodologies have been developed to simulate flow over bodies that, in general, do not conform to the computational grid. These include methods such as the immersed interface method [5], the Cartesian grid method [6] and the cut-cell method [7]; many of these variants are listed and briefly described in the review by Mittal and Iaccarino [8].

Despite the favorable features connected with the adoption of Cartesian grids, those approaches find their main drawback in the treatment of the boundary conditions: since, in fact, in the presence of irregular boundaries the truncation error tends to increase locally, the global accuracy of the spatial discretization can easily be compromised.

In this work, a novel methodology is presented for the Direct Numerical Simulation of fully-developed, buoyancy-induced flow and heat transfer in open or partially confined periodic domains containing immersed cylindrical bodies, aligned with one grid direction (x), of arbitrary cross-section. The continuity, Navier-Stokes and Energy equations are treated in their conservative form, and discretized by means of the Finite Volume method on Cartesian grids which are homogeneous along x and periodic and non-uniform along the two normal directions (y and z). Second-order time and space discretization schemes are used, and pressure-velocity coupling is achieved by means of a Projection Method. The numerical resolution of the discrete equations is carried out by means of efficient and highly parallel direct solvers.

The representation of arbitrarily irregular cylindrical boundaries on Cartesian grids is based on a modification of the original scheme developed by [9] for pure diffusion problems. The technique involves a local modification of the 5-point computational stencil where boundary segments intersect the stencil arms. The variables on the modified stencil are mapped on the global grid, by means of a linear operator determined by geometrical features and boundary conditions. The overall accuracy of the method is virtually preserved, as well as the computational efficiency of the Cartesian approach.

Verification and validation of the numerical procedure is performed. The selected test case is the flow of a fluid with $Pr = 1$ around an array of vertically-mounted, uniformly heated cylindrical rods arranged in a square lattice. A grid sensitivity analysis is performed for the case of laminar flow at $Re_\tau = 17$, for both forced and buoyancy-induced convection. Results in turbulent flow conditions at at $Re_\tau = 170$ are reported, with a focus on grid dependence.

2. Mathematical formulation

The methodology implements a discretization of the the incompressible Navier-Stokes and energy equations. The Boussinesq approximation is enforced, all the fluid properties being consistently assumed as constant, apart from density in the buoyancy term.

2.1. Continuity equation

Under the above hypotheses, the continuity equation reads:

$$\frac{\partial u_i}{\partial x_i} = 0 \tag{1}$$

2.2. Momentum equation

A formulation of momentum equations is

$$\rho \left(\frac{\partial u_i}{\partial t} + u_j \frac{\partial u_i}{\partial x_j} \right) = -\frac{\partial p}{\partial x_i} + \mu \frac{\partial^2 u_i}{\partial x_j \partial x_j} + \rho g_i \tag{2}$$

where u_i indicates the i-th component of the velocity field and the repeated index notation is implied.

The Boussinesq approximation is used in equation (2) to represent the buoyancy force

$$\rho g_i = \rho^o g_i - \rho^o g_i \beta^o \left(T - T^o\right) \tag{3}$$

where the superscript "o" denotes reference conditions.

Equation (3) can be conveniently splitted introducing the mean temperature over a y, z plane $\overline{T}_m(x)$

$$\rho g_i = \rho^o g_i - \rho^o g_i \beta^o \left[T - \overline{T}_m(x)\right] - \rho^o g_i \beta^o \left[\overline{T}_m(x) - T^o\right] \tag{4}$$

As in the case of fully developed flow with imposed heat flux, the temperature profile in axial direction is linear, equation (4) can be set as

$$\rho g_i = \rho^o g_i - \rho^o g_i \beta^o \left[T - \overline{T}_m(x)\right] - \rho^o g_i \beta^o a (x - x^o) \tag{5}$$

In equation (5), a denotes the temperature slope in x, which may be evaluated from an energy balance

$$a = \frac{q'' \omega}{\dot{m} c_p} \tag{6}$$

In equation (6), q'' indicates the imposed wall heat flux over perimeter ω, while $\dot{m}$ is the mass flow rate

$$\dot{m} \equiv \int_\Omega \rho^o u \, \mathrm{d}\Omega \tag{7}$$

and Ω is the cross section.

The first and the third terms in equation (5) may be incorporated into the pressure field giving place to a modified pressure[1]

$$p_m \equiv p - \rho^o g_1 x_1 + \rho^o g_1 \beta^o a \frac{(x_1 - x^o)^2}{2} \tag{8}$$

In fully developed conditions, the time averaged streamwise gradient of the modified pressure is constant [10]. As soon as pure natural convection conditions are considered, such a constant equals zero.

Without loss of generality, we can then split the modified pressure in a linear part P_m, depending on the streamwise coordinate only, and a fluctuation p'_m:

$$p_m(x, y, z) = P_m(x) + p'_m(x, y, z) \tag{9}$$

The pressure gradient term becomes then:

$$-\nabla p_m = -\nabla p'_m - \gamma \tag{10}$$

where γ denotes the constant pressure gradient due to external forcing of the flow. If $\gamma = 0$, pure natural convection conditions are recovered, and the fluctuating pressure field p'_m is periodic.

The fluid excess temperature is defined as

$$\theta(x, y, z) = \left[T(x, y, z) - \overline{T}_m(x)\right] \tag{11}$$

In fully developed conditions, $\overline{\theta}$ is independent of the streamwise coordinate [11].

[1] As soon as the first coordinate is directed in streamwise direction $x_1 = x$ and also gravity is directed along x, ($g_1 = -g$, $g_2 = 0$, $g_3 = 0$)

The form of the momentum equations to be solved is then

$$\rho^o \left(\frac{\partial u_i}{\partial t} + u_j \frac{\partial u_i}{\partial x_j} \right) = -\frac{\partial p'_m}{\partial x_i} + \mu \frac{\partial^2 u_i}{\partial x_j \partial x_j} + \rho^o g \beta \theta - \gamma \tag{12}$$

Using the following temperature and velocity scales in terms of the length scale L_{ref}

$$T_{\mathrm{ref}} = \frac{q''\ L_{\mathrm{ref}}}{\lambda} \qquad u_{\mathrm{ref}} = u_\tau = \sqrt{\tau_w / \rho^o} \tag{13}$$

the dimensionless momentum equation writes in terms of dimensionless quantities

$$\frac{\partial u_i^*}{\partial t^*} + u_j^* \frac{\partial u_i^*}{\partial x_j^*} = -\frac{\partial p_m^*}{\partial x_i^*} + \frac{1}{\mathrm{Re}_\tau} \frac{\partial^2 u_i^*}{\partial x_j^* \partial x_j^*} + \frac{\mathrm{Gr_q}}{\mathrm{Re}_\tau^2} \theta^* + \frac{\omega^*}{\Omega^*} \tag{14}$$

In equation (14), the friction Reynolds number Re_τ is defined as:

$$\mathrm{Re}_\tau = \frac{u_\tau\, L_{\mathrm{ref}}}{\nu} \tag{15}$$

The Grashof number $\mathrm{Gr_q}$ is also introduced, based on the imposed heat flux q'':

$$\mathrm{Gr_q} = \frac{g \beta q''\ L_{\mathrm{ref}}^4}{\lambda \nu^2} \tag{16}$$

2.3. Energy equation
As from equations (11) and (6)

$$\frac{\partial T}{\partial x} = a + \frac{\partial \theta}{\partial x}; \qquad \frac{\partial^2 T}{\partial x^2} = \frac{\partial^2 \theta}{\partial x^2} \tag{17}$$

The energy equation becomes

$$\rho^o c_p \left[\frac{\partial \theta}{\partial t} + u_i \frac{\partial \theta}{\partial x_i} \right] = \lambda \frac{\partial^2 \theta}{\partial x_i \partial x_i} - \rho^o c_p a u_1 \tag{18}$$

It is worthy to point out the appearance of the term $\rho^o c_p a u_1$ at the right-hand side of equation (18), emerging from the normalization of temperature [10].

Using the same reference quantities as for the momentum equation the energy equation writes in its dimensionless form

$$\frac{\partial \theta^*}{\partial t^*} + u_i^* \frac{\partial \theta^*}{\partial x_i^*} = \frac{1}{\mathrm{Re}_\tau \mathrm{Pr}} \frac{\partial^2 \theta^*}{\partial x_i^* \partial x_i^*} - \frac{1}{\mathrm{Re}_\tau \mathrm{Pr}} \frac{\omega^*}{\Omega^*} \frac{u_1^*}{u_m^*} \tag{19}$$

where the Prandtl number $\mathrm{Pr} = \nu/\alpha$ expresses the ratio between the diffusivities of momentum and thermal energy.

3. Numerical method

The numerical technique adopted is based on a Finite Volume implementation of a second order Projection Method, following [12]. Time-discretizations of the conservation equations are performed according to a three-level scheme, which is semi-implicit (explicit in the homogeneous direction x) for the diffusive terms, and explicit Adams-Bashfort for the advective terms. Such a practice is second order accurate in time.

Spatial derivatives are approximated with second order central differences on staggered Cartesian grids, which can be non-uniform on the transverse $y-z$ plane. A fast direct resolution of the discrete momentum and energy equations at each time-step is made possible by means of Approximate Factorization, while the Poisson problem associated with the pressure-velocity coupling [12] is solved through a fast Poisson solver, based on Matrix Decomposition [13].

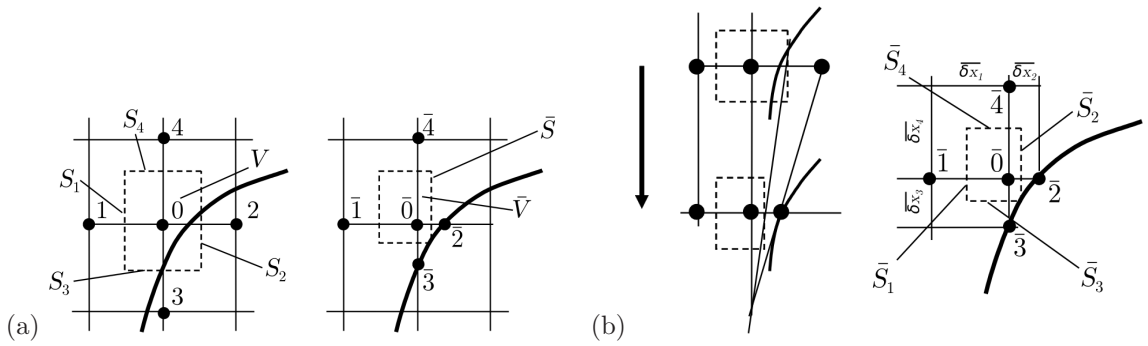

Figure 1. Treatment of irregular boundaries: (a) local stencils g (left) and d (right); (b) local cell resizing (left) and metrics of a boundary cell (right)

3.1. Treatment of irregular boundaries

The methodology employed for the modeling of boundaries non-aligned with the Cartesian grid is briefly outlined here. It represents an extension to convection problems of an algorithm which was originally developed for thermal diffusion problems [9].

On a generic plane along the x direction, in the vicinity of a boundary, two different computational stencils are defined: the stencil g belonging to the global Cartesian grid, and the stencil d, referring to the modified discretization grid, which takes into account the presence of the boundary (Figure 1a). The g stencil is complete only when all its nodes lie inside the domain, otherwise it cannot provide a complete support to the discretization of the equations, because of the "lack" of some of its nodes. Stencil d instead is always complete, since it replaces the missing nodes with the intersection points of the boundary with the grid. If all the nodes of g are internal to the domain, the two stencils coincide.

Two distinct control volumes are identified for the two stencils. The cell V is related to the computational stencil g, and its size depends only on the structure of the grid to which it refers. On the contrary, the size of the discretization cell $\bar{V}$, linked to the d-stencil, is defined coherently with the presence of the geometric boundary: the lenghts of the half-sides of $\bar{V}$ are sized as proportional to those of V, by the ratio between the distance of the cell center from the intersection point, and the length of the associated stencil arm (Figure 1b).

In general, the value of the variables $\bar{f}_k$ on stencil d can be expressed as a linear combination of the values of the nodal unknowns f_k of stencil g, plus a non-homogeneous term accounting for the boundary conditions. Hence, in vector notation, one can write:

$$\bar{\mathbf{f}} = \mathbf{E} \cdot \mathbf{f} + \mathbf{g} \tag{20}$$

If the stencil is completely contained within the domain, it is $\bar{\mathbf{f}} = \mathbf{f} \quad \Rightarrow \quad \mathbf{E} = \mathbf{I}$, $\mathbf{g} = \mathbf{0}$:

At the generic intersection node k (Figure 2), the boundary condition for the unknown f_k is expressed by the following general form:

$$a_k f_k + b_k \frac{\partial f_k}{\partial \eta_k} = c_k \tag{21}$$

where η_k denotes the direction normal to the boundary at node k. With reference to Figure 2, the index k' identifies the symmetric of node k with respect to the center of the stencil:

$$\begin{cases} k' = 3 - k & k = 1, 2 \\ k' = 7 - k & k = 3, 4 \end{cases} \tag{22}$$

By performing a second-order Taylor expansion of φ around k, along the direction η, one can

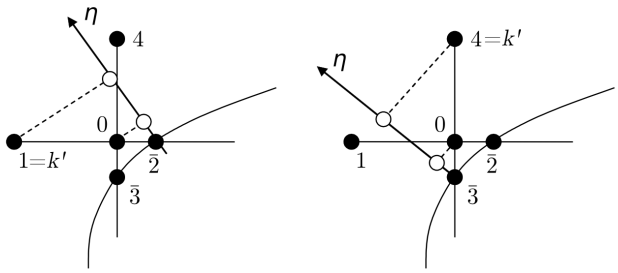

Figure 2. Local discretization stencils for different types of intersections

write:

$$\varphi(\eta) \simeq \varphi_{\eta=0} + \left(\frac{\partial\varphi}{\partial\eta}\right)_{\eta=0}\eta + \left(\frac{\partial^2\varphi}{\partial\eta^2}\right)_{\eta=0}\eta^2 \tag{23}$$

Here, the node k is taken as the origin of the η axis. The expression (23) holds for any point in the vicinity of k, and, therefore, it can be applied to all the three points 0, k, k' chosen for the approximation of the normal derivative:

$$f_l \simeq f_k + \left(\frac{\partial\varphi}{\partial\eta}\right)_{\eta=0}\eta_l + \left(\frac{\partial^2\varphi}{\partial\eta^2}\right)_{\eta=0}\eta_l^2 \quad l = 0, k, k' \tag{24}$$

On the basis of the relationship (24), the normal derivative of the variable φ at the boundary can be expressed as a linear combination of the nodal values of the variable itself in the points 0, k, k' of the stencil:

$$\begin{aligned}\left(\frac{\partial\varphi}{\partial\eta}\right)_{\eta=0} &= p_{k,0}\bar{f}_0 + p_{k,k}\bar{f}_k + p_{k,k'}\bar{f}_{k'} = \\ &= \sum_l p_{k,l}\bar{f}_l, \quad l = 0, k, k'\end{aligned} \tag{25}$$

The coefficients $p_{k,l}$ can be determined by substituting equation (24) into equation (25) and then enforcing congruence between the members of the resulting equations.It is then possible to insert the expression (25)into the generic boundary condition (21), thus obtaining:

$$a_k\bar{f}_k + b_k\sum_l p_{k,l}\bar{f}_l = c_k, \qquad l = 0, k, k' \tag{26}$$

Equation (26) expresses a useful constraint to determine the value of f_k, when point k lies on the boundary. If, on the contrary, the computational stencil is completely contained within the domain, one simply has $\bar{f}_k = f_k$. Hence, a general equation can be written as follows:

$$(a_k + b_k p_{k,k})\bar{f}_k + b_k\sum_{l=0,l\neq k}^{4} p_{k,l}\bar{f}_l = c_k + d_k f_k \tag{27}$$

where $d_k = 1$ if the associated node is inside the domain, while $d_k = 0$ if the node lies on the boundary. Equation (27) can be reformulated in matrix notation as:

$$\mathbf{A}\cdot\bar{\mathbf{f}} = \mathbf{D}\cdot\mathbf{f} + \mathbf{c} \tag{28}$$

It is now possible to formulate the expressions for $\mathbf{E}$ and $\mathbf{g}$ introduced by the definition (20):

$$\mathbf{E} = \mathbf{A}^{-1}\cdot\mathbf{D}, \qquad \mathbf{g} = \mathbf{A}^{-1}\cdot\mathbf{c} \tag{29}$$

It should be noted that the values of $\mathbf{E}$ and $\mathbf{g}$ depend only on the coefficients of equation (21) and on the boundary geometry and, therefore, they can be calculated once for all in the pre-processing phase of the numerical procedure.

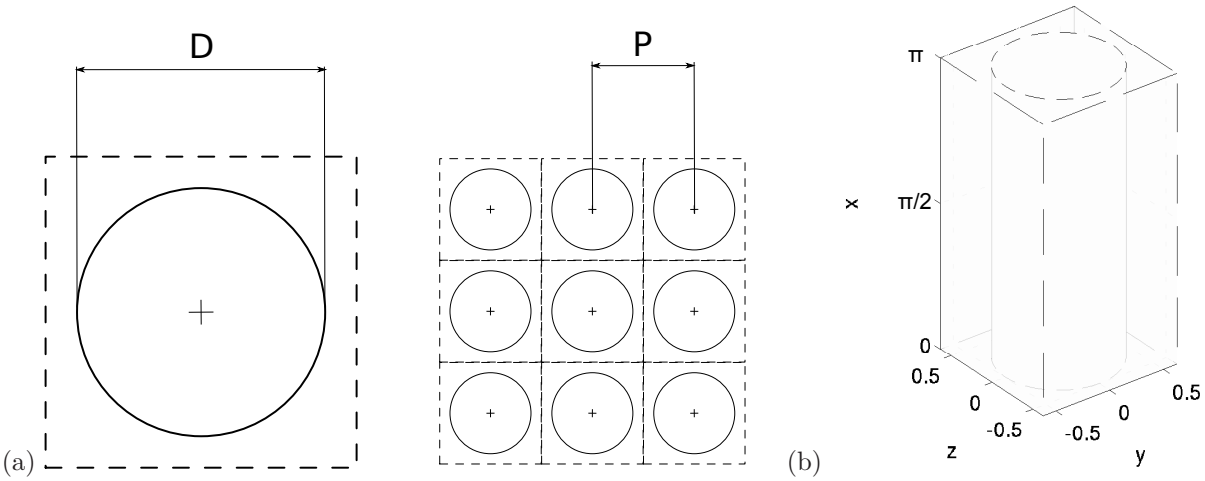

Figure 3. Unit cell of a square array of rods: cross section (a) and vertical development (b)

3.2. Parallel implementation

Parallelism is introduced using the message-passing library MPI. As mentioned above, the momentum and energy equations are made explicit in the homogeneous direction x; for the solution of the momentum and energy equations a one-dimensional domain decomposition is thus implemented in x.

A Fourier decomposition method is applied for solving the Poisson equation, which arises at every time step for the enforcement of mass conservation [12]

$$\nabla^2\phi = \nabla \cdot \mathbf{u} \tag{30}$$

Thus a one-dimensional Fourier expansion is performed along x followed by the solution of a two dimensional Poisson equation in each y, z plane.

4. Verification and validation

Verification and validation of the numerical method has been performed on the case schematised in Figure 3. A square lattice of cylindrical rods of diameter D, each heated with a uniform heat flux density q'', whose centers are spaced by pitch P, is represented by its unit cell (Figure 3a). In fully-developed conditions, the rod bundle is thought to have an infinite extension along the streamwise, vertical direction x. The computational domain is thus $L_x = \pi$, $L_y = L_z = P$ in the streamwise and the cross-flow directions, respectively (Figure 3b). The physical situation of a bundle of heated rods under the hypothesis of fully developed flow and heat transfer can be represented through periodic conditions, which are enforced on the velocity field, the modified pressure field p_m and the modified temperature-like variable θ along all coordinate directions [14].

As discussed in Ref. [15], from a practical standpoint, the flow induced by buoyancy in a bundle of heated rods is always associated with a non-zero mean flow and a pressure drop, since typically the heat source is of finite height, and it is inserted in a loop together with a suitable cooling section. Such is the situation, for instance, of DHR loops in nuclear applications. Hence, the flow under consideration, although being induced solely by buoyancy, cannot be viewed as a purely natural convection flow, since, in that case, the hypothesis of full development would entail a zero mean flow rate and pressure drop. This apparent paradox is solved by inserting a forcing term in equation (18) which realizes a fully developed mixed convection flow, representative of the actual flow inside a bundle of heated rods.

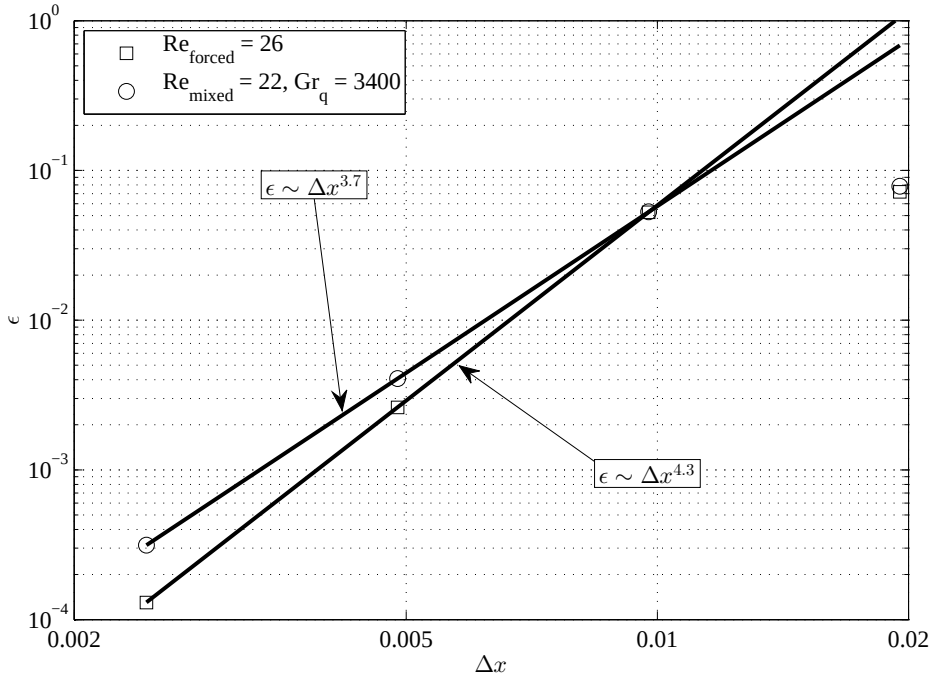

Figure 4. Grid independence test: deviation ϵ from the continuum value vs. Δx.

4.1. Grid independence test

Grid independence is assessed in laminar flow conditions by considering both forced and mixed convection conditions, for $\mathrm{Pr} = 1$. A value $\mathrm{Re}_\tau = 17$ is chosen for the forced convection case, which determines a Reynolds number $\mathrm{Re}_{\mathrm{forced}} = 26$; a value $\mathrm{Gr}_\mathrm{q} = 3.4 \times 10^3$ is then set for the mixed convection case, so that $\mathrm{Gr}_\mathrm{q}/\mathrm{Re}^2 = \mathcal{O}(1)$, in order to match the experimental findings of El Genk et al. [16]. The resulting Reynolds number for the mixed case is $\mathrm{Re}_{\mathrm{mixed}} = 22$.

Four different grids with constant spacing are used, with a refinement ratio of 2 along the y and z directions (see Table 1). The average Nusselt number on the rod surface is chosen as the reference quantity for assessing grid convergence. Richardson extrapolation [17] was then performed on the results of the three finest grids to determine an estimate of the continuum value, and the order of convergence of the grid. Figure 4 reports the absolute deviation ϵ from the continuum value as a function of the grid spacing Δx, along with an indication of the order of convergence p in the grid independent region. For both cases, $p \sim 4$, indicating an excellent grid convergence.

Table 1. Grid independence test for $\mathrm{Re}_\tau = 17$ and $\mathrm{Gr}_q = 3.4 \times 10^3$

n. of elements	Δx	$\mathrm{Nu}_{\mathrm{forced}}$	$\mathrm{Nu}_{\mathrm{mixed}}$
64^2	0.0195	4.79	5.68
128^2	0.0098	4.77	5.65
256^2	0.0049	4.73	5.60
512^2	0.0024	4.72	5.60
$\to \infty$	$\to 0$	4.72	5.60

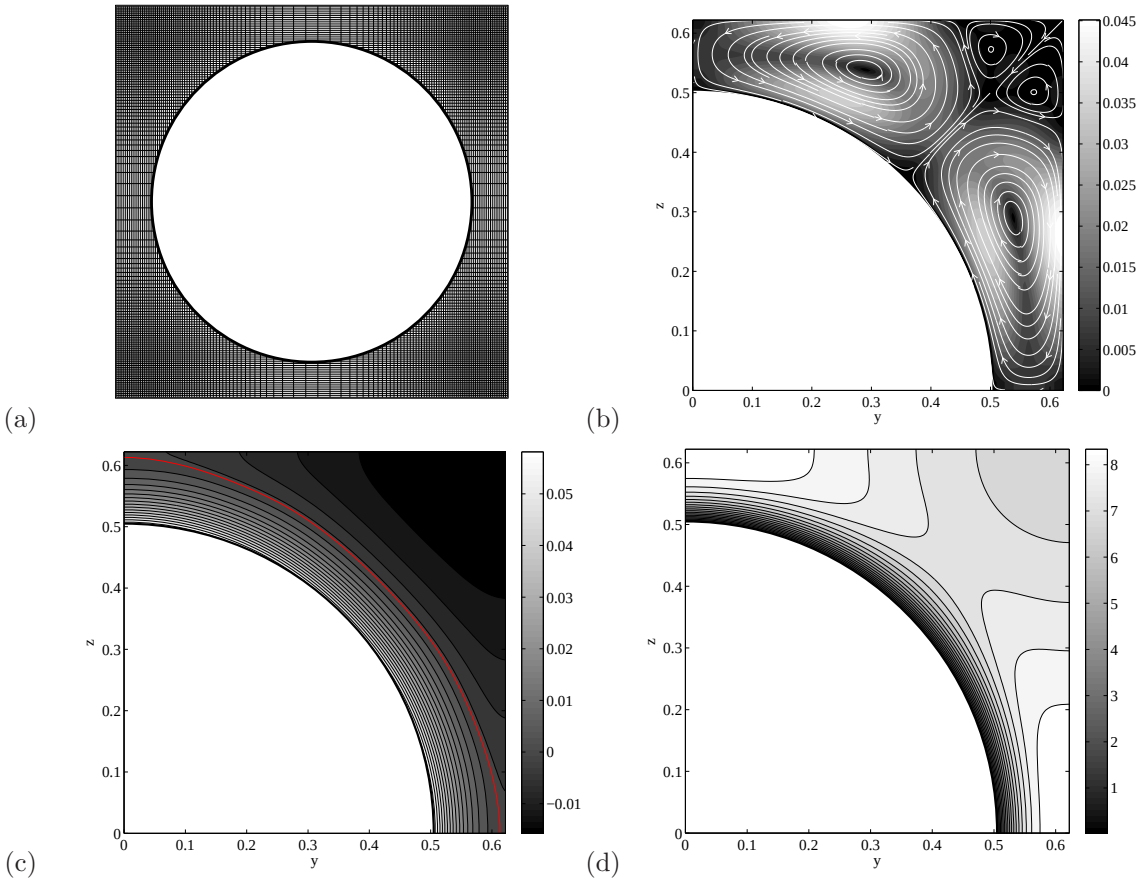

Figure 5. Turbulent flow at $\mathrm{Re}_\tau = 170$, $\mathrm{Gr_q} = 1.32 \times 10^7$, $\mathrm{Pr} = 1$: (a) cross section of the 128^3 computational mesh; (b) streamlines and magnitude of the mean secondary flow components; contours of time-averaged (c) θ and (d) u_x.

4.2. Results in turbulent conditions

Direct Numerical Simulations of fully developed, turbulent, buoyancy-induced flow are performed for $\mathrm{Re}_\tau = 170$, $\mathrm{Gr_q} = 1.32 \times 10^7$, on two different grids. The coarser mesh includes 128^3 elements (see Figure 5a), while the finer counts 256^3 cells.

Non-zero time-averaged secondary flow components are detected. As displayed in Figure 5b, four symmetric vortices are found; two of them are small and very weak $|u_y| \sim |u_z| \sim 0.01 u_{x,\max}$.

Contours of the time-averaged normalized temperature θ and of the time-averaged streamwise velocity component are displayed in Figure 5c and 5d. The peak mean velocity is in $y = P/4, z = 0$ and $y = 0, z = P/4$, while $\overline{u}_x$ decreases towards $y = P/4, z = P/4$, this can be explained by the negative momentum source associated with a negative $\overline{\theta}$. The normalized temperature is negative around $y = P/4, z = P/4$ but becomes positive close to the heated walls. The red line in figure 5 indicates the $\overline{\theta} = 0$ isotherm line. The sign of the time averaged source of momentum changes when

$$\frac{\mathrm{Gr_q}}{\mathrm{Re}_\tau^2}\theta^* = -\frac{\omega^*}{\Omega^*} \tag{31}$$

where $\frac{\mathrm{Gr}}{\mathrm{Re}_\tau^2} \approx 457$ and $\frac{\omega^*}{\Omega^*} \approx 4.04$ in our case.

Profiles of $\overline{u_x}$, $\overline{\theta}$, Reynolds stresses and turbulent heat fluxes across the large $d_l = 0.768D$ gap at a 45^o angle with respect to the y and z axes (Figure 6a) show that the velocity field

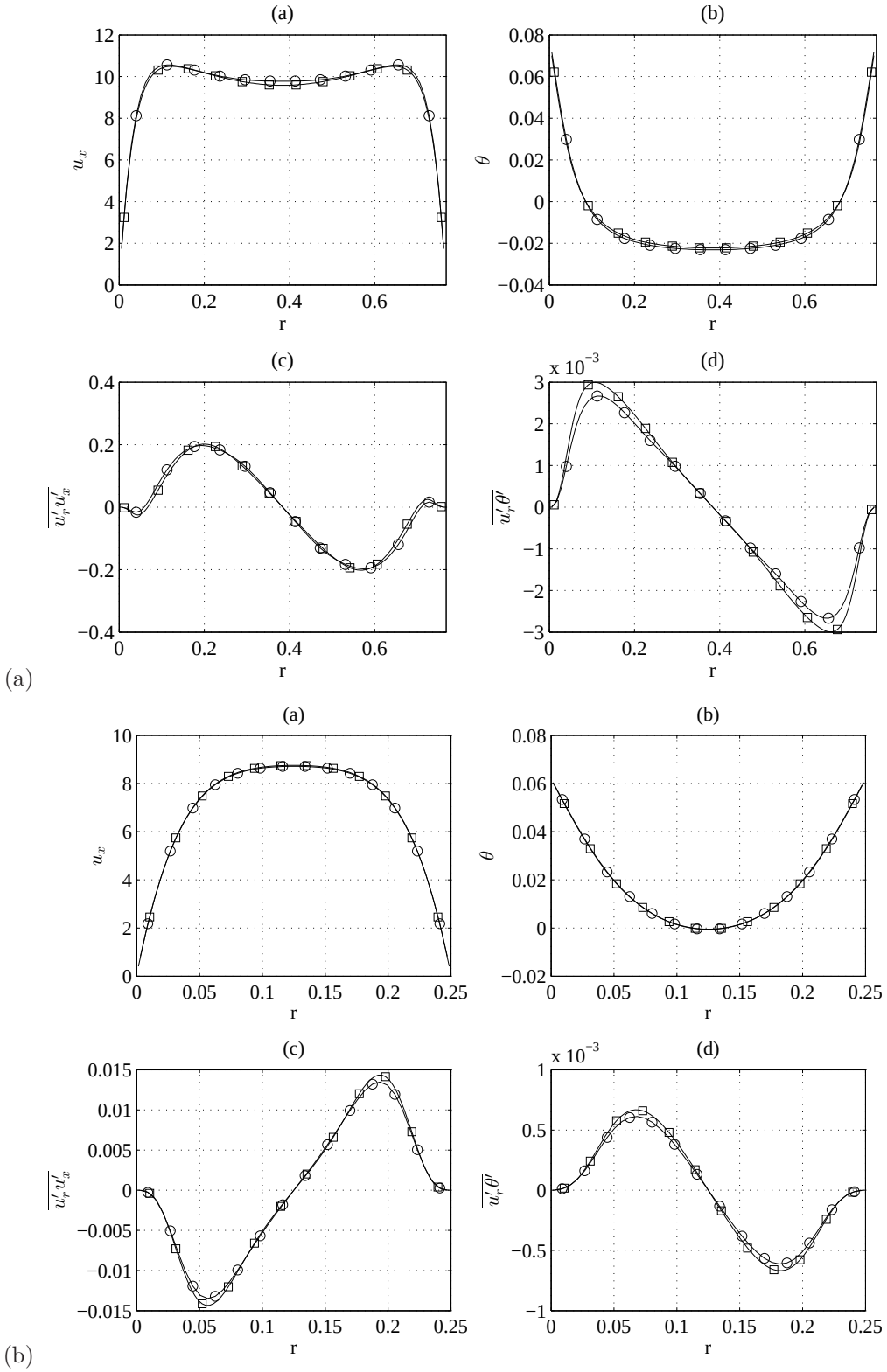

Figure 6. Turbulent flow at $\mathrm{Re}_\tau = 170$, $\mathrm{Gr_q} = 1.32 \times 10^7$, $\mathrm{Pr} = 1$: profiles of (a) $\overline{u_x}$, (b) $\overline{\theta}$, Reynolds stresses and turbulent heat fluxes across the $d_l = 0.768D$ (a) $d_n = 0.5D$ (b) gaps. Circles and squares indicate results for the 128^3 and 256^3 grid, respectively.

is characterized by two peaks and a central minimum; accordingly Reynolds stresses display two positive peaks and two negative peaks. Across the $d_n = 0.5D$ horizontal and vertical gap (Figure 6b) the profile of the velocity field displays one single, central peak and due to the smaller integral length scale associated with domain dimensions, the turbulent flow characteristics are weaker with respect to Figure 6a.

5. Concluding remarks

A novel technique has been presented, for the Direct Numerical Simulation of buoyancy-induced flows in open or partially confined periodic domains, containing immersed cylindrical bodies. A grid sensitivity analysis has been performed for the case of laminar flow around a square lattice of heated rods. Grid independence tests, based on the average Nusselt number in laminar conditions, suggest that the procedure ensures grid convergence. Results in the weakly turbulent regime display almost laminar characteristics when plotted along the larger, $0.768D$ gap. Across the same gap, the velocity profile displays two peaks; accordingly the Reynolds stress are characterized by four extrema. Across the smaller, $0.5D$ gap the mean velocity is maximum in the center despite the forcing term reaches its minimum in that location. Results in turbulent conditions also highlight that mean quantities and first-order moments have a reduced dependence from the grid. The proposed methodology represents a powerful tool for the analysis of buoyancy-induced turbulent convection in many configurations.

Acknowledgements

The research leading to these results has received funding from the Euratom research and training programme 2014-2018 under grant agreement No 654935 (SESAME).

References

[1] Moin P and Mahesh K 1998 *Annual Review of Fluid Mechanics* **30** 539–578
[2] Lee M and Moser R D 2015 *Journal of Fluid Mechanics* **774** 395–415
[3] Yokokawa M, Itakura K, Uno A, Ishihara T and Kaneda Y 2002 *Procs. ACM/IEEE SC '02 Conf.* pp 1–17
[4] Peskin C 2002 *Acta Numerica* **11** 479–517
[5] Leveque R J and Li Z 1994 *SIAM Journal on Numerical Analysis* **31** 1019–1044
[6] Patankar S V 1978 *Proc. 6th Int. Heat Transfer Conf.* vol 3 p 297
[7] Leveque R 1988 *Journal of Computational Physics* **78** 36–63
[8] Mittal R and Iaccarino G 2005 *Annual Review of Fluid Mechanics* **37** 239–261
[9] Barozzi G S, Bussi C and Corticelli M A 2004 *Numerical Heat Transfer B* **46** 56–77
[10] Piller M and Stalio E 2012 *International Journal of Heat and Mass Transfer* **55** 6506–6513
[11] Patankar S, Liu C and Sparrow E 1978 *International Journal of Heat and Mass Transfer* **21** 557–566
[12] Gresho P M 1990 *International Journal for Numerical Methods in Fluids* **11** 587–620
[13] Babu V and Korpela S 1993 *Journal of Computational Physics* **104** 93–98
[14] Piller M, Nobile E and Hanratty T 2002 **458** 419–441
[15] Hallinan K and Viskanta R 1985 *International Journal of Heat and Fluid Flow* **6** 256–264
[16] El-Genk M, Su B and Guo Z 1993 *International Journal of Heat and Mass Transfer* **36** 2359–2374
[17] Roache P J 1972 *Computational Fluid Dynamics* 1st ed (Hermosa)